Evolution of Substructure of a Non-equiatomic FeMnCrCo High Entropy Alloy Deformed at Ambient Temperature

A.K. CHANDAN, S. TRIPATHY, M. GHOSH, and S.G. CHOWDHURY

The present investigation aims at discerning the evolution of microstructure of a $Fe_{40}Mn_{40}Cr_{10}Co_{10}$ high entropy alloy, under uni-axial loading at room temperature. At the time of quasi-static uni-axial loading, the alloy exhibited an ultimate tensile strength of ~ 514 MPa with fracture strain of ~ 47 pct. Multiple stages of work hardening were observed during the deformation. The initial work hardening of the alloy, for the true strain of ε ~ 0.05 to 0.1, was facilitated by the rigorous planar slip of dislocations. Extensive cell formation in the mid-strain levels, i.e., for ε ~ 0.1 to 0.29, resulted in overall softening. The onset of microband formation was also observed during the mid-strain level, which further got populated in large numbers during the final stage of deformation. Simultaneous occurrence of twins as well as deformation induced FCC → HCP phase transformation was observed in the grains oriented along TD//⟨111⟩ in the fractured specimen. Highly dense dislocation walls were also found at strain $\varepsilon \geq 0.29$. The alloy showed an overall increase in work hardening before fracture, which was ascribed to the occurrence of twins, FCC → HCP phase transformation, microbands, and highly dense dislocation walls.

I. INTRODUCTION

HIGH Entropy Alloy (HEA) is a new class of engineering materials, which offer a wide spectrum for alloy design, versatile microstructure, and unique properties. Since their advent more than a decade ago,[1–3] HEAs produced through various routes have shown attractive properties over conventional engineering materials, such as ultrahigh fracture toughness,[4] excellent combination of strength and ductility,[5–7] high hardness,[8,9] and adequate corrosion resistance.[8,9] Unlike the conventional alloys, which generally consist of one principal element, HEAs are multiple principal element system (MPES). MPESs consisting of all or some of the transition elements like Fe, Mn, Cr, Co and Ni in various combinations have been investigated extensively. This huge focus is driven by the novel mechanical properties shown by such MPESs as compared to the established engineering materials. In this context, Gludovatz et al.[4] reported that the equiatomic CrMnFeCoNi alloy displayed extraordinary damage tolerance with tensile strengths > 1 GPa, fracture toughness > 200 MPa $m^{1/2}$ at crack initiation and ~ 300 MPa $m^{1/2}$ for stable crack growth at 77 K. Deformation behavior and mechanical properties of the equiatomic CrMnFeCoNi alloy are available in open domain literature.[4,7,10–13] Several compositional derivatives of the equiatomic CrMnFeCoNi alloy were also investigated and demonstrated encouraging mechanical properties.[13–22]. In this regard, the equiatomic CrCoNi alloy showed superior tensile properties and fracture toughness than the equiatomic CrMnFeCoNi alloy both at the room and cryo temperatures.[17,19,21] The fine-grain equimolar FeCrCoNi alloy wires displayed tensile yield strength of ~ 1.2 GPa at 223 K.[20] Recently, Bae et al.[14] reported a non-equiatomic $Fe_{60}Co_{15}Ni_{15}Cr_{10}$ (at. pct) alloy which displayed an extraordinary combination of tensile properties with the ultimate tensile strength of ~ 1.5 GPa and ductility ~ 87 pct at 77 K.

A relatively more cost-effective non-equiatomic alloy, $Fe_{40}Mn_{40}Cr_{10}Co_{10}$ (at. pct) was presented by Deng et al. which possessed the room temperature tensile properties comparable to the established twinning induced plasticity (TWIP) steels.[22] The alloy revealed nano twinning mediated deformation in comparison to the absence of twin formation in the equiatomic CrMnFeCoNi alloy at room temperature.[7] The concept behind the alloy design was to reduce the stacking fault energy (SFE)

A.K. CHANDAN and S. TRIPATHY are with the Academy of Scientific and Innovative Research (AcSIR), Ghaziabad, 201002, India and also with the Materials Engineering Division, CSIR National Metallurgical Laboratory, Jamshedpur, 831007, India. M. GHOSH and S.G. CHOWDHURY are with the Materials Engineering Division, CSIR National Metallurgical Laboratory. Contact e-mail: ghosh_mnk@yahoo.com, mainakg@nmlindia.org

by removing Ni along with suitable adjustment of other four elements. This alteration in the SFE might facilitated nano twin formation even during room temperature deformation. The strain hardening of the alloy, facilitated by the nano twins, indicated its high aptness for the structural applications. It was shown that the nano twins occurred at low strain level of ~ 10 pct.[22] However, the work hardening rate ($d\sigma/d\varepsilon$) was found to decrease continuously with the deformation of the material.[22] Therefore, the propensity of occurrence of nano twins during the deformation and its role in providing the effective work hardening needs to be assessed carefully. Moreover, it is noteworthy that the tensile tests carried out by Deng *et al.* included the miniature tensile specimens of the dimension $10 \times 2.5 \times 1$ mm.[22] Before the efficacious use, it is also necessary to confirm the size effect of specimen toward the evolution of microstructural characteristics for any new alloy system.

In this perspective, the current study presents the evolution of microstructure of $Fe_{40}Mn_{40}Cr_{10}Co_{10}$ alloy, deformed in uni-axial tensile loading at a strain rate of 10^{-4} s^{-1}. The starting microstructure of the alloy in the present investigation possessed larger grains as compared to the previous report.[22] Microstructural characterization has been carried out on samples deformed at different strain levels. The characteristic features are corroborated with the strain hardening behavior of the alloy.

II. EXPERIMENTAL DETAILS

The alloy was prepared by vacuum arc melting with the final composition (atomic pct) 40Fe-40Mn-10Cr-10Co. The ingot was re-melted five times in order to ensure compositional homogeneity. The cast ingot was homogenized at 1200 °C for 2 hours, followed by forging into ~ 80 mm diameter disc with 8 mm final thickness. The disc was air cooled to room temperature. A small sample was selected from the forged disc. The sample was polished properly, cleaned in running water and followed by sonication in ultrasonic bath of acetone. The bulk composition was measured by energy dispersive spectroscopy at 15 Kv for ×100 magnification. The tabulated data (Table I) are the average of five such readings, obtained from different locations.

Rectangular sections (45 mm × 30 mm) were cut from the forged disc and heat treated at 1200 °C for 1 hour, followed by hot rolling at 950 °C to 65 pct reduction in thickness. The hot rolled specimens were further annealed at 1200 °C for a short duration of 15 minutes and quenched in water. Identification of phases was done by X-ray diffraction (XRD) using Cu-K$_\alpha$ radiation (Bruker D8 Advance diffractometer). XRD patterns were recorded in the Bragg–Brentano ($\theta - 2\theta$) geometry over an angular range of 40 to 105 deg (2θ) using a step size of 0.02 deg and 5 seconds dwelling time. XRD based Williamson-Hall analysis was performed in order to determine the crystallite size (D) and the microstrain in the deformed specimen.[23,24] The root

mean square strain $\left(\left\langle \varepsilon^2 \right\rangle^{\frac{1}{2}}\right)$ was calculated from the microstrain (e) using the following relation[25]:

$$\left\langle \varepsilon^2 \right\rangle^{\frac{1}{2}} = (2/\pi)^{0.5} * e \qquad [1]$$

The dislocation density (ρ) was estimated using relation between the root mean square strain $\left(\left\langle \varepsilon^2 \right\rangle^{\frac{1}{2}}\right)$ and the crystallite size (D)[26–28]:

$$\rho = 2\sqrt{3} * \frac{\left\langle \varepsilon^2 \right\rangle^{\frac{1}{2}}}{D * b} \qquad [2]$$

where, b is the Burgers vector of the dislocation.

Tensile specimens with a gage length of 25 mm were prepared from the hot rolled and annealed sheets as per the ASTM E8M-03 standards. Tensile testing was carried out at room temperature at an engineering strain rate of 10^{-4} s^{-1}. Interrupted tensile testing was also carried out at different engineering strain levels of $e = 0.1$ and 0.2. From the plane containing the tensile axis and the transverse axis of tensile tested specimens, sampling was carried out for electron backscattered diffraction (EBSD) and transmission electron microscopy (TEM) investigations. EBSD investigation was done in the FEI Quanta 3D FEG SEM equipped with TSL OIM detector. EBSD scans were performed with the step size of 0.15 μm. For TEM examination, perforation in 3 mm ϕ mechanically ground coupons was obtained by electropolishing in a 90: 10 acetic acid: perchloric acid solution. During polishing the bath temperature was ~ 10 °C with a voltage of ~ 35 V. The foils were investigated in analytical microscopes operated at 200 KV (Philips CM200 and JEOL JEM 2200FS).

III. RESULTS

A. *Initial microstructure and tensile properties*

Figure 1(a) shows the EBSD inverse pole figure (IPF) map of the as-rolled and annealed specimen, featuring equiaxed grains of the face centered cubic (FCC) phase with a significant population of annealing twins. The IPF along the tensile direction (TD) depicted a weak texture after hot rolling and annealing of the specimen (Figure 1(b)). This indicated that the grains in the specimen did not possess any preferred orientation instead it exhibited nearly random texture after the hot rolling and annealing. The grain size of the alloy, excluding the twins, was in the range of 150 to 180 μm. Figure 1(c) displays the XRD pattern of the specimen. The characteristic peaks were indexed with respect to the FCC crystal structure. Presence of any other phase other than austenite was not detected. The lattice parameter of the FCC phase was ~ 3.62 Å. Finer structural details of the same specimen is illustrated in Figure 2(a) which showed the presence of fringes corresponding to stacking fault (SF) in the rolled and annealed specimen. The image provided in Figure 2(a) is the bright field (BF)

Table I. Chemical Composition of the Alloy (At. Pct)

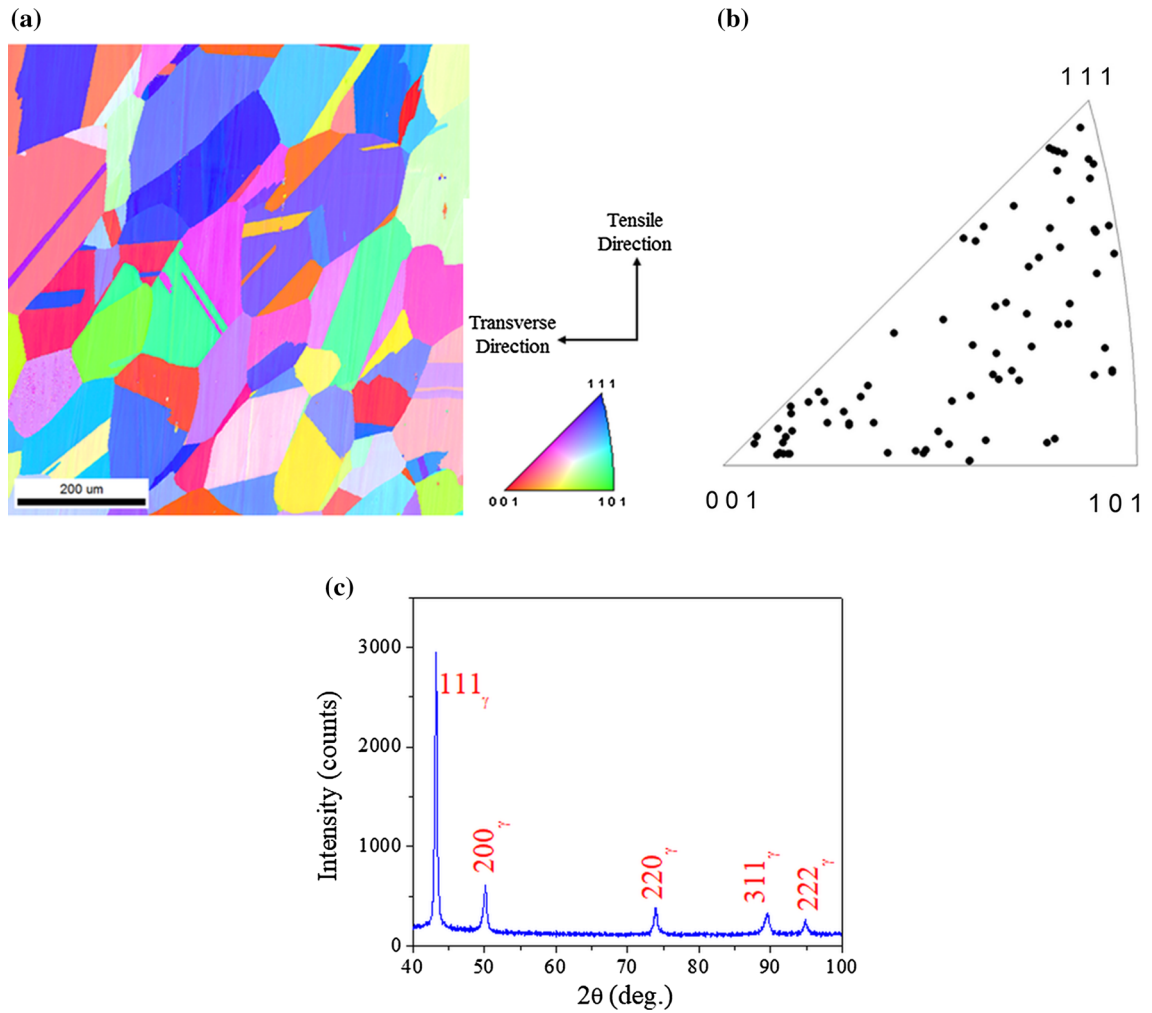| Fe	Mn	Cr	Co	C	Others
40.79 ± 1.1	39.07 ± 1.6	10.42 ± 0.7	9.53 ± 0.6	0.043 ± 0.01	rest

Fig. 1—Hot rolled and annealed specimen (*a*) EBSD IPF map (*b*) IPF along the tensile direction (TD), and (*c*) XRD pattern from the through thickness of the specimen.
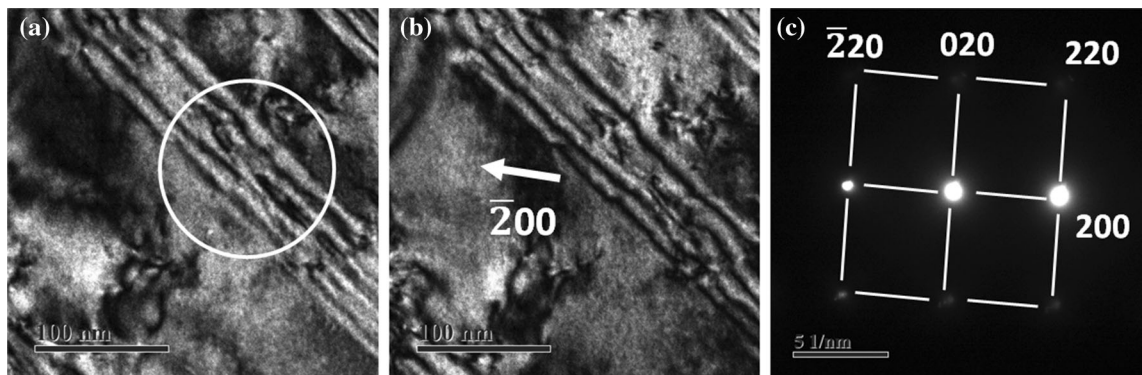

Fig. 2—Stacking fault (SF) in rolled and annealed specimen (*a*) BF image showing SF fringes and (*b*) axial DF image with $\bar{2}00$ g active, and (*c*) analyzed SAD pattern in two beam condition; SAD pattern was obtained from the encircled region of the BF image.
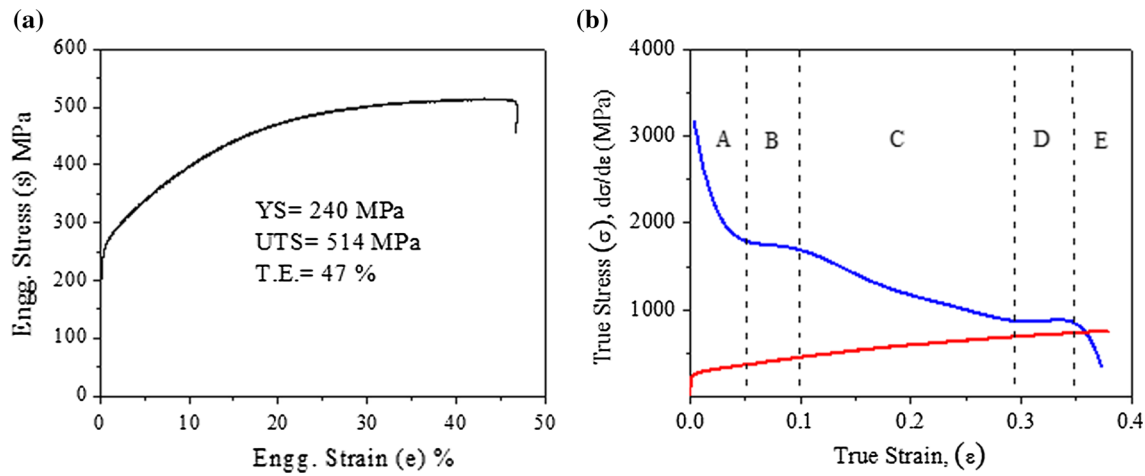
Fig. 3—Tensile properties of the alloy (*a*) engineering stress–strain curve and (*b*) true stress–strain curve along with the plot of work hardening.

image, from which the selected area diffraction (SAD) pattern was taken (encircled region) in two beam condition with 200 vector (g) being active (Figure 2(c)). From that situation, $\bar{2}00$ vector (g) was activated to obtain the axial dark field (DF) image (Figure 2(b)). As operating vector $\bar{2}00$ in the axial DF image was pointing away from the bright outer fringe (the bright outer fringe is in the extreme right of the Figure 2(b)), the stacking fault was extrinsic type (Figure 2(b)).[29] The stacking faults might have formed during the hot rolling and subsequent annealing of the specimen.

The room temperature engineering stress (s)-strain (e) response of the alloy is presented in Figure 3(a). The corresponding true stress (σ)-strain (ε) curve and the work hardening (WH) plots are shown in Figure 3(b). The alloy exhibited adequate combination of strength and ductility. The alloy displayed five stages of work hardening as marked by A, B, C, D, and E (Figure 3(b)). After an initial steep decrease in stage A (up to ε ~ 0.05), the stage B (from ε ~ 0.05 to 0.1) showed nearly a constant value of dσ/dε (work hardening rate) over a range of ε. This observation indicated some compensatory WH mechanism was active in stage B and was responsible in slowing down the decrement in the dσ/dε value with respect to stage A. In stage C (ε ~ 0.1 to 0.29), a smooth decrease in dσ/dε value was observed, followed by a marginal increase in the WH rate in stage D (from ε ~ 0.29 to 0.35). Finally, a steep fall in the WH rate was found in stage E (beyond ε ~ 0.35) up to fracture.

B. *Evolution of Microstructure During Deformation*

1. *Specimen strained up to e = 0.1*

Figures 4(a) and (b) depict the IPF map and IPF along the TD of different grains of the specimen deformed up to e = 0.1. This envisaged that the grains were oriented in such a fashion that the TD became aligned along the ⟨001⟩ to ⟨101⟩ crystallographic axes of the grains in the specimen. Further, the specimen

displayed intersecting planar arrays of dislocation to form a checkerboard type arrangement (Figure 5(a)). This was an example of the activation of limited slip systems in the matrix during deformation. The nearly straight dislocation lines represented planar slip on two different {111} planes.[30–33] The angle between the intersecting dislocation lines was ~ 70 deg, which was also the angle between the family of {111} planes. This observation endorsed that slip occurred in two different {111} planes during the early stage of the deformation and can be largely responsible for work hardening in stage B.[22,34] Dislocation entanglement without any preferred configuration was also present signifying the occurrence of wavy slip (Figure 5(b)). The wavy slip was the manifestation of dislocation cross slip and is generally found in materials with medium to high SFE.[35,36] Cross slip of the screw components of dislocations resulted in the entanglement of dislocations. This wavy slip of dislocation might trigger the formation of cell structure in the later part of deformation.[35–39] Nano twins were scanty in this specimen (Figures 5(c) and (d)). The formation of nano twins during deformation was a signature of materials with low to medium SFE.

2. *Specimen strained up to e = 0.2*

EBSD and TEM investigation of the specimen deformed up to e = 0.2 revealed an overall qualitative increase in the dislocation density. The absolute value of the same was ~ 3 × 10^{14} m^{-2} and ~ 16 × 10^{14} m^{-2} for engineering strain (= e) of ~ 0.1 and ~ 0.2, respectively. Furthermore, no significant change in the propensity of twins was observed. In dearth of sufficient deformation induced dislocation obstacles (such as twins), the dislocation density and its mobility increased to accommodate the plastic strain within the material. The increase in the dislocation mobility and density perhaps steered the evolution of various dislocation substructure. Extensive cross slip of screw dislocations took place to yield well-developed dislocation cells in the specimen strained up to e = 0.2 (Figure 6(a)).[35–39] Cross slip of
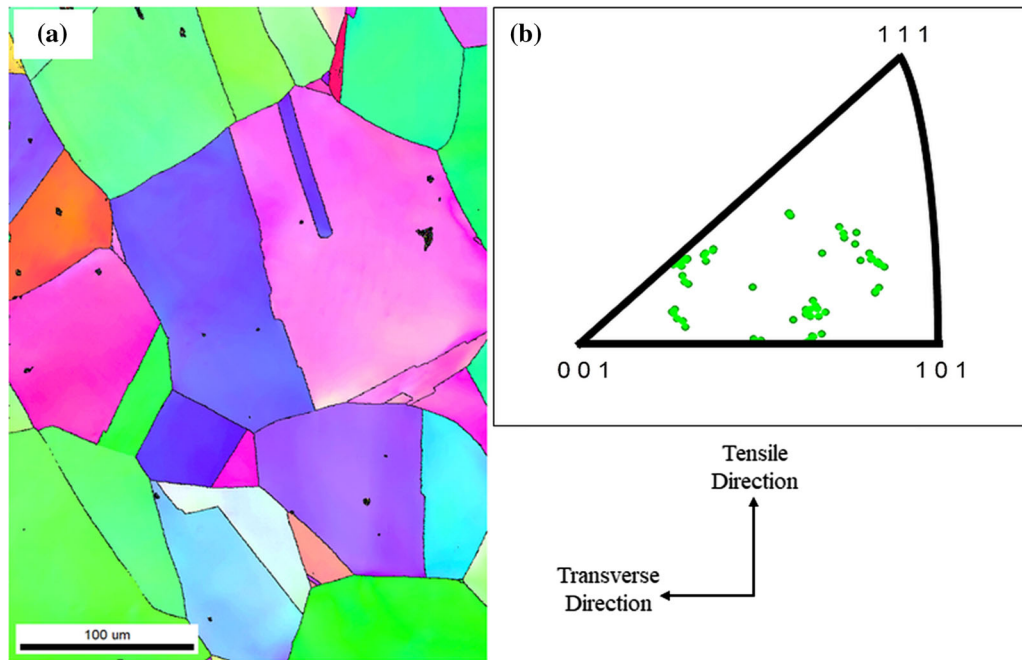
Fig. 4—Reorientation of grains during deformation (*a*) IPF map and (*b*) IPF along the TD of different grains for the specimen deformed up to *e* = 0.1.
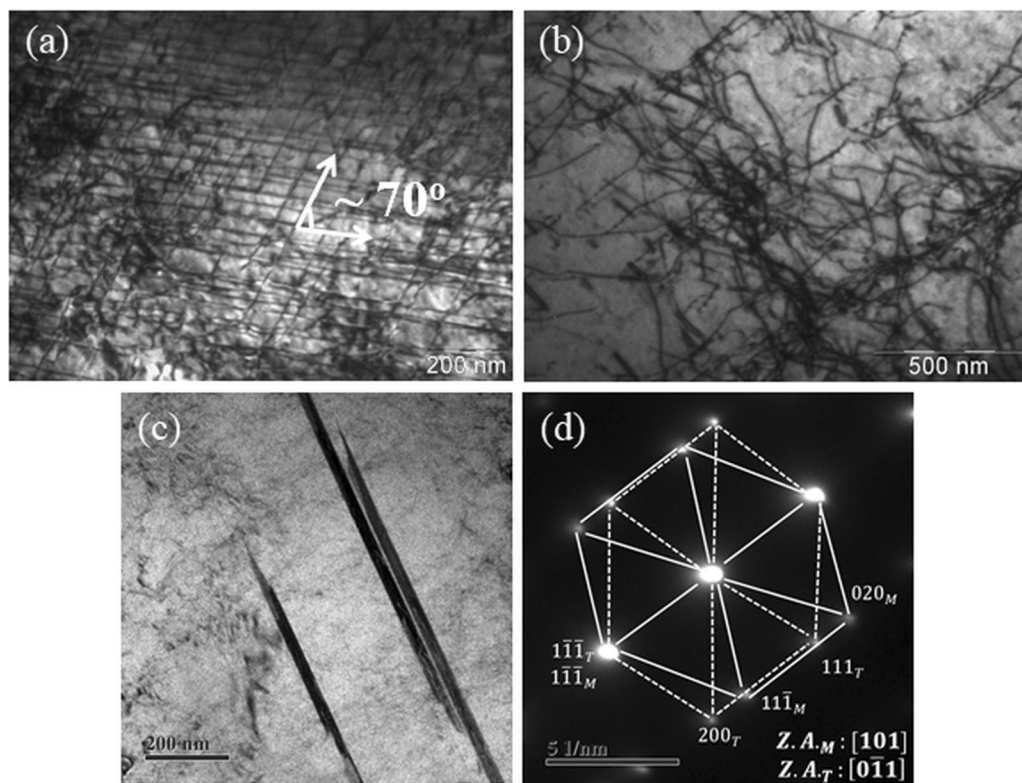

Fig. 5—TEM images of specimen deformed up to *e* = 0.1 (*a*) planar slip of dislocations in the specimen along with intersecting slip lines in two different {111} planes, (*b*) wavy slip of dislocations, (*c*) deformation induced nano twins, and (*d*) the corresponding analyzed SAD pattern.

dislocations is a stress assisted process[40] and is promoted in FCC alloys by high SFE and high mobility of dislocations.[41] Since the present alloy is not a high SFE

FCC system,[22] the formation of dislocation cells was mainly prompted by the high dislocation mobility and high stress application (*e* = 0.2). The average size of the
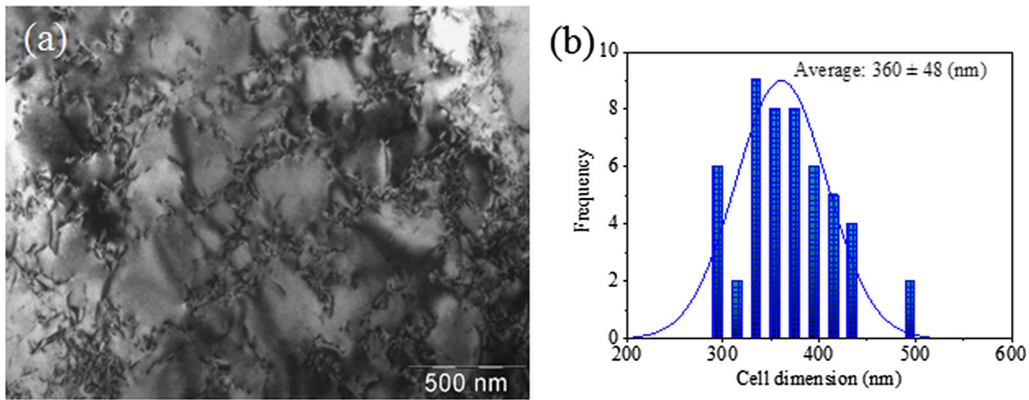
Fig. 6—Appearance of dislocation cells in the specimen deformed up to $e = 0.2$ (*a*) BF TEM micrograph and (*b*) size distribution of such cells.
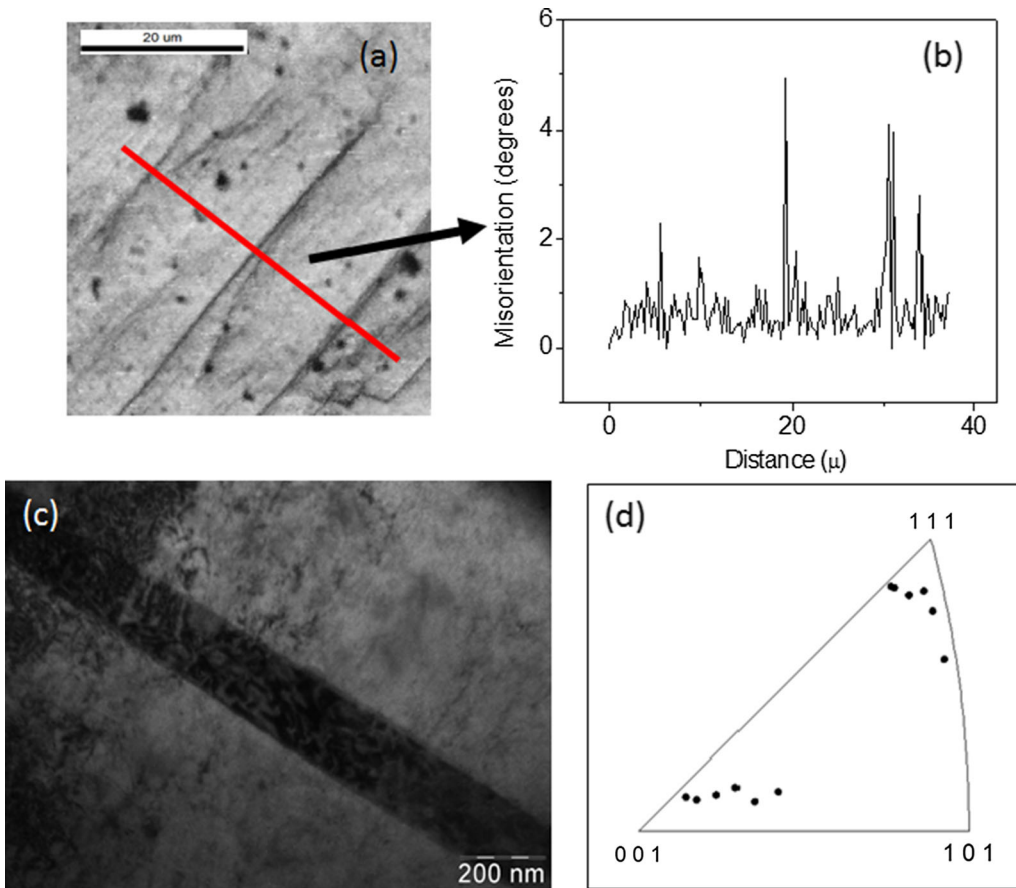

Fig. 7—Microbands and their characteristics in the specimen deformed up to $e = 0.2$ (*a*) EBSD image quality map from a selected region of a grain containing diffuse bands, (*b*) misorientation profile crossing one of the bands, (*c*) BF TEM micrograph of a microband, and (*d*) IPF along the TD of different grains containing microbands.

dislocation cell was calculated considering at least ten TEM images to obtain a statistically reliable data and found to be ~ 360 ± 48 nm (Figure 6(b)).

Additionally, the thin diffused deformation bands were also revealed in the EBSD investigation (Figure 7(a)). These bands could possibly be the microbands, as the misorientation profile (point to point) across the bands was low (3 to 5 deg)

(Figure 7(b)) and were limited within the grains.[42] The TEM investigation confirmed the presence of such microbands (Figure 7(c)). The microband formation was facilitated under the prevailing condition of planar glide (Figure 5(a)) with restricted slip systems. In that situation the activation of other slip systems was energetically unfavorable.[43] The EBDS analysis further discerned that the microband formation was triggered in

the grains oriented along $\langle 001 \rangle$//TD and $\langle 111 \rangle$//TD (Figure 7(d)).

3. *Fractured specimen*

Increment in work hardening rate was observed after stage C as indicated before the fracture (Figure 3(b)). TEM investigation revealed co-existence of twining (T) and the hexagonal close packed (HCP) phase (ε) (Figures 8(a) and (c)). As depicted in Figure 8(c), the FCC matrix (M) and the HCP phase maintained the orientation relationship as,[44]

$$[011]_\gamma \| [2\bar{1}\bar{1}0]_\varepsilon$$

$$(\bar{1}1\bar{1})_\gamma \| (000\bar{2})_\varepsilon$$

The appearance of HCP phase in the microstructure was an example of FCC $\rightarrow$ HCP transformation during deformation for low SFE alloys, which reflected the WH mechanism called transformation induced plasticity (TRIP) effect.[41,45,46] The occurrence of successive

bands of twins and HCP phase reduced the effective mean free path of the dislocations. A significant entrapment of dislocations within the bands was evident in Figure 8(a).

EBSD analysis also endorsed twinning and formation of HCP phase in the deformed microstructure. Intensive deformation twins were depicted in the image quality map (Figure 9(a)). The misorientation profile across couple of twins within a grain was shown in Figures 9(b) and (c). The misorientation of 60 deg about $\langle 111 \rangle$ axis clearly indicated the existence of primary deformation twinning in the fractured specimen. Both TEM and EBSD analysis revealed that twin and HCP phase occurred together in same grains with orientation along $\langle 111 \rangle$//TD. This implied that the same orientation under uni-axial tensile condition facilitated the formation of both twins and HCP phase. This became more evident from the IPF map and the image quality map of a grain oriented along $\langle 111 \rangle$//TD (Figures 10(a) and (b)). Figure 10(c) is the IPF along TD where the same was obtained from regions near the twins. Figure 10(d) is obtained from those regions close to HCP phase. The
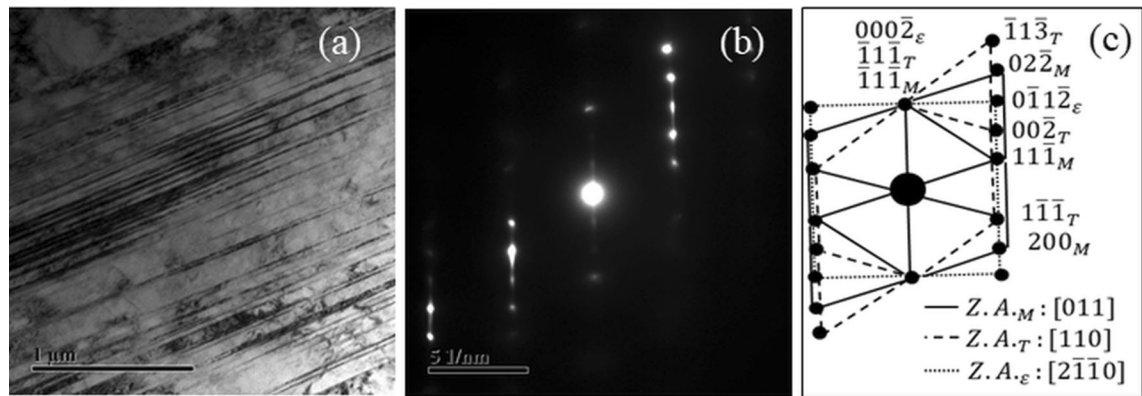

Fig. 8—Evolution of microstructure in the fractured specimen (*a*) BF TEM micrograph showing cluster of deformation twins (T) and ε- HCP in the FCC matrix (M), (*b*) corresponding SAD pattern, and (*c*) schematic of the indexed SAD pattern.
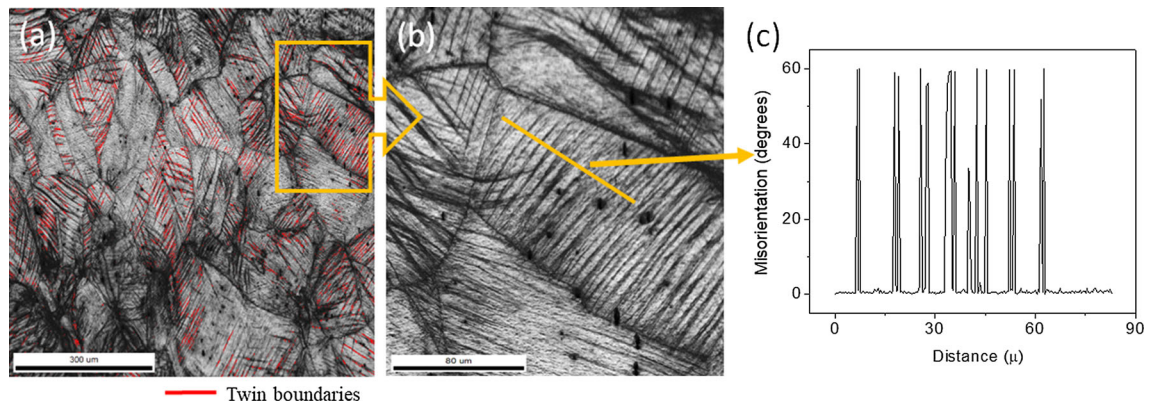

Fig. 9—Planar defects in the fractured specimen (*a*) EBSD image quality map showing occurrence of deformation twins, marked with red lines, (*b*) image quality map from of a selected region and (*c*) misorientation profile across the line crossing the deformation twins.
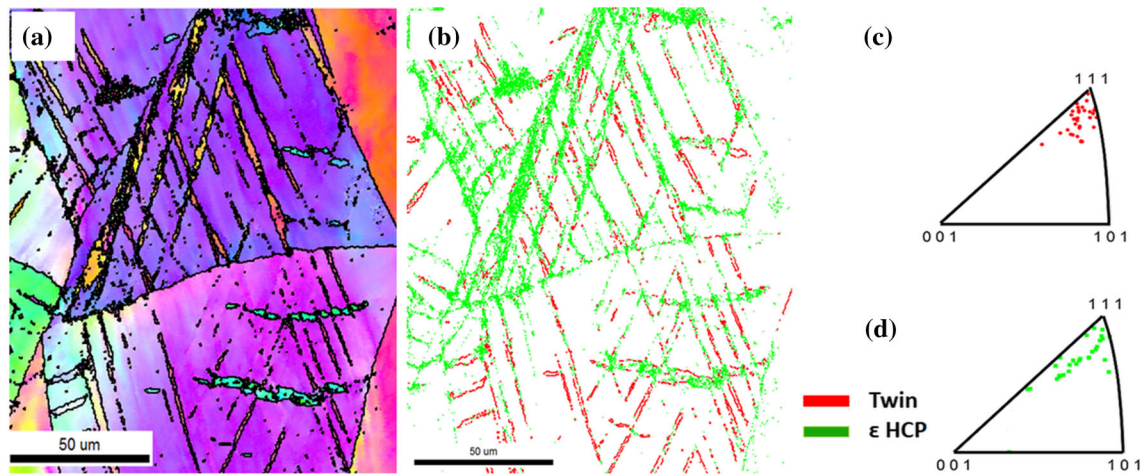
Fig. 10—Formation of twins and HCP phase within a grain oriented along TD//⟨111⟩ in the fractured specimen (a) IPF of the selected area, (b) IQ map showing deformation twins (red) and HCP phase (green) and (c) IPF from grains containing twins and (d) IPF from grains containing HCP phase. (In Figs. 10(b) and (d), the red color represents the twins, while the green color indicates the HCP phase).
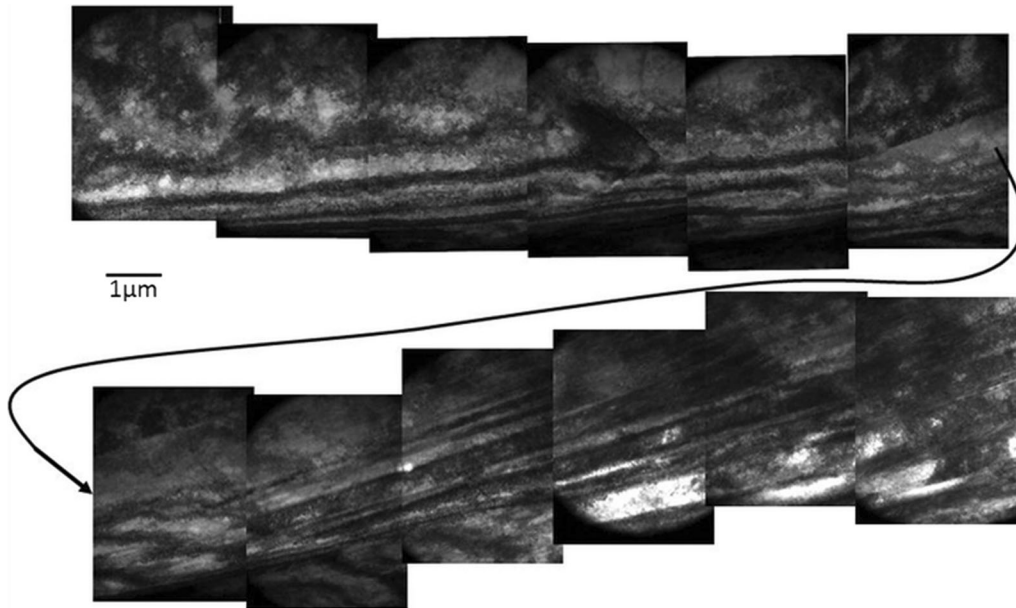

Fig. 11—Montage of series of TEM images exhibiting several HDDWs over a single grain.

volume fraction of the deformation induced HCP phase and twins in the Figure 10 was determined from EBSD and found to be ~ 9 pct and ~ 5 pct, respectively.

Additionally, highly dense dislocation walls (HDDWs) were abundant in most of the grains. The length of such HDDWs was found as high as ~ 50 μ. Figure 11 is a montage of TEM micrographs representing few full-length HDDWs formed over a single grain. The HDDWs were found to interact with twins (Figure 12(a)). Further, it was evident from Figure 12(b) that qualitatively the number density of microbands was increased substantially in the fractured specimen. An enhancement in the strength and ductility can also be achieved by the grain subdivisions produced by the formation and intersection of microbands.[43]

IV. DISCUSSION

The hot rolled alloy displayed a satisfactory combination of strength and ductility at room temperature. In comparison to the equiatomic CrMnFeCoNi alloy (YS ~ 360 MPa for 4.4 μm grain size), the low yield strength (~ 240 MPa) of the present alloy can be attributed to the initial coarse grain structure.[7] It was expected that the solid solution strengthening effect would be reduced in the present alloy with the decrease in the alloy content as compared to the equiatomic CrMnFeCoNi. However, comparing with the similar grain size, the present system exhibited an improvement in YS than the equiatomic CrMnFeCoNi system (YS ~ 170 MPa for 155 μm grain size).[7] This was an indication that solid solution
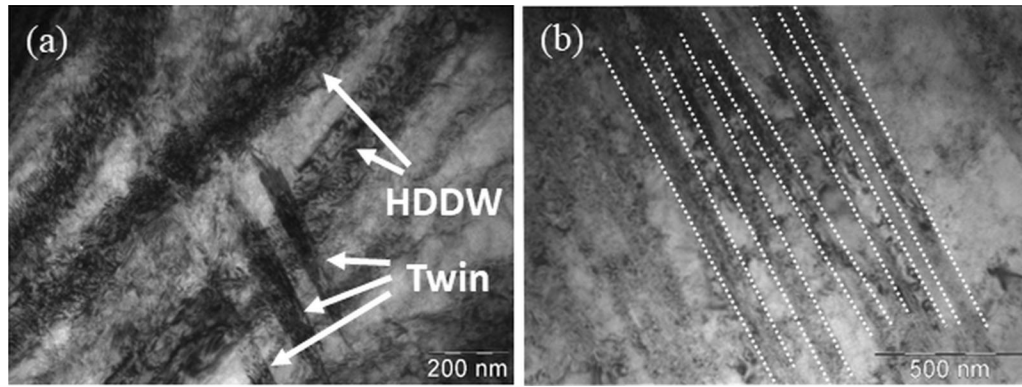
Fig. 12—TEM micrographs of fractured specimen exhibiting (*a*) intersection of HDDWs and twins and (*b*) densely populated microbands (marked by dotted lines).

Table II.   Maximum Schmid Factor for Dislocation Slip and Mechanical Twinning in Different Orientations

Orientation	Schmid Factor	
	Twinning	Slip
$\langle 111 \rangle$	0.41	0.24
$\langle 101 \rangle$	0.41	0.47
$\langle 001 \rangle$	0.27	0.31

strengthening was not the major strengthening mechanism in the present alloy.

A. *Evolution of Deformation Microstructure*

The initial orientation of the grains with respect to the TD indicated a weak texture in the hot rolled specimen (Figure 1(b)). The grains, however, was observed to get reoriented during tensile loading. The initial weak texture eventually became sharp at early stage of deformation such that the TD was aligned along the $\langle 001 \rangle$ to $\langle 101 \rangle$ oriented grains for the specimen deformed up to $e = 0.1$ (Figure 4). The reorganization of grains favored extensive slip during this stage (Figures 5(a) and (b)). The predominance of slip could be explained on the basis of high Schmid factor for slip as compared to the twinning. Table II presents the maximum Schmid factor values for differently oriented grains along the TD.[34] The Schmid factor for slip in the grains oriented along $\langle 001 \rangle$//TD direction was high as compared to that for twinning to occur. Furthermore, the high Schmid factor for twinning as compared to slip in the grains oriented along $\langle 101 \rangle$//TD direction signified the occurrence of twinning in such grains. However, in the present case, the qualitative number density of grains oriented along $\langle 101 \rangle$//TD direction were less and therefore the propensity of the twinning was also small in the specimen deformed up to $e = 0.1$. Moreover, formation of twins in the microstructure requires dislocation slip as an essential prerequisite event.[47–49] Hence, it was expected that the tendency of twinning

might increase after adequate extent of dislocation slip *i.e.*, at the later part of deformation. Simultaneous occurrence of deformation characteristics pertaining to SFE ranging from low to high SFE regimes was observed in the present alloy (Figure 5). The co-existence of deformation features associated with both low to medium and medium to high SFE materials are common in FCC alloys.[5,7,34,39,41,50] In this context, grain orientation is also an important factor, which can control the deformation behavior apart from SFE. The orientation dependence of deformation characteristics has been widely discussed in literature.[22,39,51–53] The orientation dependency of defects formation is evident in the present case. The appearance of slip assisted deformation such as planar and wavy slips occurred in the grains oriented along $\langle 001 \rangle$//TD. Nano twins occurred in the grains oriented along $\langle 101 \rangle$//TD.

In the specimen deformed up to $e = 0.2$, the grain orientation along $\langle 001 \rangle$//TD favored the formation of microbands (Figure 7(d)). Furthermore, it has been shown that the formation of dislocation cells to be restricted in grains with orientation $\langle 001 \rangle$//TD, having the highest Schmid factor for slip among all the orientations.[22] This signifies that the plastic strain in the specimen deformed up to $e = 0.2$ was accommodated by the occurrence defect substructures like dislocation cells (Figure 6) and microbands (Figure 7) in the grains favorably oriented for slip along $\langle 001 \rangle$//TD.

It is well recognized that extensive slip is required for the nucleation and growth of twins.[47–49] Thus, the twin density was increased considerably in the fractured specimen after a significant extent of slip during the early stage of deformation. The IPF of the fractured specimen illustrated that the grains containing deformation twins in the fractured specimen were oriented along $\langle 111 \rangle$//TD (Figure 10(c)). This characteristic endorsed that the higher Schmid factor for twinning than for slip in the grains oriented along $\langle 111 \rangle$ (Table II) facilitated extensive twinning such grains. Further, it is noteworthy that the grains with orientation along $\langle 111 \rangle$//TD also favored the formation of strain-induced HCP phase in the fractured specimen (Figure 10(d)). The occurrence of twinning requires coordinated movement of schokley partials on the {111} plane.[54,55] The
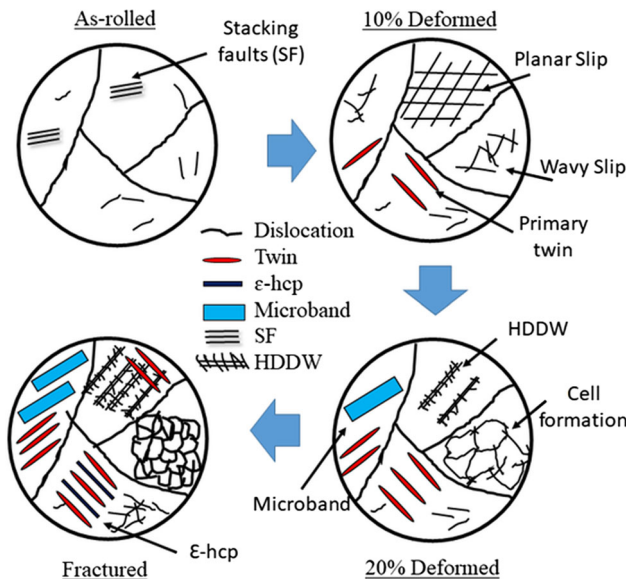
Fig. 13—Schematic presentation of the sequential evolution of structural constituents during tensile deformation of the alloy.

appearance of twins in high propensity at higher strain levels in the grains oriented along $\langle 111 \rangle$//TD, suggested that the formation and movement of schokley partials became easy as compared to that of the perfect dislocations. The formation of the HCP phase requires faulting in the stacking sequence on every second {111} plane[56–58] and each faulting could be associated with the formation of schokley partials. Therefore, the easy formation and movement of schokley partials in the grains with orientation along $\langle 111 \rangle$//TD might also propelled the HCP phase formation. Furthermore, the presence of extrinsic type stacking faults in the initial hot rolled and annealed microstructure also steered the occurrence of HCP phase. Idrissi et al.[59] have shown that the extrinsic stacking faults in the FCC austenite phase acted as nucleation sites for the HCP ε-martensite in a Fe-Mn-Al-Si alloy.

The overall deformation sequence in the present system can be illustrated by following schematic presentation (Figure 13).

B. Work Hardening of the Alloy

It is evident from Figure 3(b), that the present alloy exhibited multiple stages of work hardening. Occurrence of various deformation characteristics during tensile loading contributed to the work hardening of the specimen (Table III). Initial steep decrease in the work hardening rate in stage A was associated with the dynamic recovery processes such as cross slip, annihilation of dislocations with opposite sign and formation of low energy dislocation substructures.[60] The nearly steady state work hardening in stage B was due to slip of planar dislocations along with the onset of twinning. However, it was noteworthy that, the occurrence of wavy slip might have resulted in decreased work hardening.[34] Nevertheless, the contribution of wavy

Table III. Mechanisms Operative in Different Stages of Work Hardening

Work Hardening Stage	True Strain Level	Deformation Characteristics	Net Effect
Stage A	~ 0 to 0.05	dynamic recovery processes such as cross slip, annihilation of dislocations with opposite sign and formation of low energy dislocation substructures	initial softening
Stage B	~ 0.05 to 0.1	rigorous planar slip beginning of cross slip appearance of few nano twins	planar array of dislocations resulted in work hardening
Stage C	~ 0.1 to 0.29	increased dislocation density extensive cross slip leading to dislocation cell formation appearance of microbands low density of nano twins	overall softening induced by cross slip of dislocations
Stage D	~ 0.29 to 0.35	high density of nano twins increased presence of microbands deformation induced FCC to HCP phase transformation presence of high dislocation density walls	work hardening just before fracture of the specimen

slip was considerably less as compared to the planar slip of the dislocations, which facilitated an overall steady work hardening rate during deformation in the stage B. The specimen showed an overall decrease in the work hardening in stage C. This decrease in the work hardening rate was due to the increased cross slip of dislocations, leading to cell formation.[34,41,50] The cross slip of dislocations was consequence of the increased dislocation density and high mobility of the same.[41] The microbands and twins did not provide a significant contribution to the work hardening in stage C due to their meager population. Further, the alloy exhibited an increment in the work hardening in stage D. Evidently, severe twinning and HCP phase formation along with the presence of HDDWs and microbands were collectively responsible for providing work hardening at higher strain levels before fracture.

From the above investigation, it becomes obvious that the present alloy with relatively larger grain size as compared to the previous study showed a couple of significant differences in the deformation behavior.[22] One of them was the strain-induced FCC → HCP phase transformation during the deformation. Secondly, the occurrence of microbands at mid-strain level and fractured specimen was not found in earlier report in the present alloy. Therefore, exploration of sub-micro structural constituents at each stage of deformation may open up a domain to play with alloy design to improve its mechanical properties further.

V. CONCLUSION

The present investigation highlights the evolution of deformation structure and the concomitant contribution of the same toward the work hardening for a multiple principal element system, $Fe_{40}Mn_{40}Cr_{10}Co_{10}$, during the uni-axial tensile deformation. The major findings are summarized below:

- The present alloy provides a satisfactory combination of strength (~ 514 MPa) and ductility (elongation to fracture ~ 47 pct). The alloy showed multiple stages of work hardening which involved the evolution of various dislocation substructure, planar faults, and deformation induced phase transformation.
- The initial stage of work hardening (from ε ~ 0.05 to 0.1) was facilitated by the planar slip of dislocations along with the onset of deformation nano twins.
- The mid-stage of deformation (from ε ~ 0.1 to 0.29) was featured by softening effect, induced by the extensive cell formation. Formation of nano twins and microbands could not contribute much to the work hardening due to their small population.
- The alloy finally illustrated an increase in work hardening which was attributed to the occurrence of deformation twins, microbands, highly dense dislocation walls, and transformation induced plasticity.

REFERENCES

1. J.W. Yeh, S.K. Chen, S.J. Lin, J.Y. Gan, T.S. Chin, T.T. Shun, C.H. Tsau, and S.Y. Chang: *Adv. Eng. Mater.*, 2004, vol. 6, pp. 299–303.
2. B. Cantor, I.T.H. Chang, P. Knight, and A.J.B. Vincent: *Mater. Sci. Eng. A*, 2004, vols. 375–377, pp. 213–18.
3. S. Ranganathan: *Curr. Sci.*, 2004, vol. 85, pp. 1404–06.
4. B. Gludovatz, A. Hohenwarter, D. Catoor, E.H. Chang, E.P. George, and R.O. Ritchie: *Science*, 2014, vol. 345, pp. 1153–58.
5. Z. Li, K.G. Pradeep, Y. Deng, D. Raabe, and C.C. Tasan: *Nature*, 2016, vol. 534, pp. 227–30.
6. Y. Brif, M. Thomas, and I. Todd: *Scr. Mater.*, 2015, vol. 99, pp. 93–96.
7. F. Otto, A. Dlouhý, C. Somsen, H. Bei, G. Eggeler, and E.P. George: *Acta Mater.*, 2013, vol. 61, pp. 5743–55.
8. Y.L. Chou, J.W. Yeh, and H.C. Shih: *Corros. Sci.*, 2010, vol. 52, pp. 2571–81.
9. Y.Y. Chen, U.T. Hong, H.C. Shih, J.W. Yeh, and T. Duval: *Corros. Sci.*, 2005, vol. 47, pp. 2679–99.
10. C.C. Tasan, Y. Deng, K.G. Pradeep, M.J. Yao, H. Springer, and D. Raabe: *JOM*, 2014, vol. 66, pp. 1993–2001.
11. B. Schuh, F. Mendez-martin, B. Völker, E.P. George, H. Clemens, R. Pippan, and A. Hohenwarter: *Acta Mater.*, 2015, vol. 96, pp. 258–68.
12. G. Laplanche, A. Kostka, O.M. Horst, G. Eggeler, and E.P. George: *Acta Mater.*, 2016, vol. 118, pp. 152–63.
13. A. Gali and E.P. George: *Intermetallics*, 2013, vol. 39, pp. 74–78.
14. J. Wung, J. Bok, J. Moon, S. Su, M. Ji, H. Yong, B. Lee, and H. Seop: *Acta Mater.*, 2018, vol. 161, pp. 388–99.
15. Y. Wang, B. Liu, K. Yan, M. Wang, S. Kabra, Y. Chiu, D. Dye, P.D. Lee, Y. Liu, and B. Cai: *Acta Mater.*, 2018, vol. 154, pp. 79–89.
16. C.E. Slone, S. Chakraborty, J. Miao, E.P. George, M.J. Mills, and S.R. Niezgoda: *Acta Mater.*, 2018, vol. 158, pp. 38–52.
17. J. Miao, C.E. Slone, T.M. Smith, C. Niu, H. Bei, M. Ghazisaeidi, G.M. Pharr, and M.J. Mills: *Acta Mater.*, 2017, vol. 132, pp. 35–48.
18. Z. Li and D. Raabe: *JOM*, 2017, vol. 69, pp. 2099–2106.
19. G. Laplanche, A. Kostka, C. Reinhart, J. Hunfeld, G. Eggeler, and E.P. George: *Acta Mater.*, 2017, vol. 128, pp. 292–303.
20. W. Huo, F. Fang, H. Zhou, Z. Xie, J. Shang, and J. Jiang: *Scr. Mater.*, 2017, vol. 141, pp. 125–28.
21. B. Gludovatz, A. Hohenwarter, K.V.S. Thurston, H. Bei, Z. Wu, E.P. George, and R.O. Ritchie: *Nat. Commun.*, 2016, vol. 7, pp. 1–8.
22. Y. Deng, C.C. Tasan, K.G. Pradeep, H. Springer, A. Kostka, and D. Raabe: *Acta Mater.*, 2015, vol. 94, pp. 124–33.
23. G.K. Williamson and W.H. Hall: *Acta Metall.*, 1953, vol. 1, pp. 22–31.
24. K. Jeong, J.-E. Jin, Y.-S. Jung, S. Kang, and Y.-K. Lee: *Acta Mater.*, 2013, vol. 61, pp. 3399–3410.
25. E.J. Mittemeijer and U. Welzel: *Z. Kristallogr.*, 2008, vol. 223, pp. 552–60.
26. G.K. Williamson and R.E. Smallman: *Phil. Mag.*, 1956, vol. 1, pp. 34–46.
27. R.E. Smallman and K.H. Westmacott: *Phil. Mag.*, 1957, vol. 2, pp. 669–83.
28. Y.H. Zhao, H.W. Shang, and K. Lu: *Acta Mater.*, 2001, vol. 49, pp. 365–75.
29. B. Fultz and J. Howe: *Transmission Electron Microscopy and Diffractometry of Materials*, Springer, New Yrok, 2007.
30. K.T. Park, K.G. Jin, S.H. Han, S.W. Hwang, K. Choi, and C.S. Lee: *Mater. Sci. Eng. A*, 2010, vol. 527, pp. 3651–61.

31. J.D. Yoo and K.T. Park: *Mater. Sci. Eng. A*, 2008, vol. 496, pp. 417–24.
32. F.Y. Dong, P. Zhang, J.C. Pang, Q.Q. Duan, Y.B. Ren, K. Yang, and Z.F. Zhang: *Acta Metall. Sin.*, 2016, vol. 29, pp. 140–49.
33. D. Canadinc, H. Sehitoglu, H.J. Maier, and Y.I. Chumlyakov: *Acta Mater.*, 2005, vol. 53, pp. 1831–42.
34. Y.-K. Lee: *Scr. Mater.*, 2012, vol. 66, pp. 1002–06.
35. B. Bay, N. Hansen, D.A. Hughes, and D. Kuhlmann-Wilsdorf: *Acta Metall. Mater.*, 1992, vol. 40, pp. 205–19.
36. N. Hansen and D.J. Jensen: *Philos. Trans. R. Soc. A*, 1999, vol. 357, pp. 1447–69.
37. D. Kuhlmann-Wilsdorf: *Mater. Sci. Eng. A*, 2001, vol. 315, pp. 211–16.
38. X. Huang: *Scripta Mater.*, 1998, vol. 38, pp. 1697–1703.
39. I. Gutierrez-Urrutia and D. Raabe: *Acta Mater.*, 2011, vol. 59, pp. 6449–62.
40. P.S. Follansbee and U.F. Kocks: *Acta Metall.*, 1988, vol. 36, pp. 81–93.
41. D.T. Pierce, J.A. Jiménez, J. Bentley, D. Raabe, and J.E. Wittig: *Acta Mater.*, 2015, vol. 100, pp. 178–90.
42. F.J. Humphreys and M. Hatherly: *Recrystallization and Related Annealing Phenomena*, 2nd ed., Elsevier, New York, 2004.
43. K.T. Park, G. Kim, S.K. Kim, S.W. Lee, S.W. Hwang, and C.S. Lee: *Met. Mater. Int.*, 2010, vol. 16, pp. 1–6.
44. P.L. Mangonon and G. Thomas: *Metall. Trans.*, 1970, vol. 1, pp. 1577–86.
45. C. Wang, W. Cao, J. Shi, C. Huang, and H. Dong: *Mater. Sci. Eng. A*, 2013, vol. 562, pp. 89–95.
46. Y.F. Shen, X.X. Li, X. Sun, Y.D. Wang, and L. Zuo: *Mater. Sci. Eng. A*, 2012, vol. 552, pp. 514–22.
47. J.W. Christian and S. Mahajan: *Prog. Mater. Sci.*, 1995, vol. 39, pp. 1–157.
48. T.-H. Lee, C.-S. Oh, S.-J. Kim, and S. Takaki: *Acta Mat.*, 2007, vol. 55, pp. 3649–62.
49. L. Bracke, L. Kestens, and J. Penning: *Scr. Mater.*, 2009, vol. 61, pp. 220–22.
50. I. Gutierrez-Urrutia and D. Raabe: *Acta Mater.*, 2012, vol. 60, pp. 5791–5802.
51. I. Gutierrez-Urrutia, S. Zaefferer, and D. Raabe: *Mater. Sci. Eng. A*, 2010, vol. 527, pp. 3552–60.
52. P. Yang, Q. Xie, L. Meng, H. Ding, and Z. Tang: *Scr. Mater.*, 2006, vol. 55, pp. 629–31.
53. L. Meng, P. Yang, Q. Xie, H. Ding, and Z. Tang: *Scr. Mater.*, 2007, vol. 56, pp. 931–34.
54. H. Fujita and T. Mori: *Scr. Metall.*, 1975, vol. 9, pp. 631–36.
55. S. Mahajan and G.Y. Chin: *Acta Metall.*, 1973, vol. 21, pp. 1353–63.
56. H. Fujita and S. Ueda: *Acta Met.*, 1972, vol. 20, pp. 759–67.
57. J.W. Brooks, M.H. Loretto, and R.E. Smallman: *Acta Metall.*, 1979, vol. 27, pp. 1829–38.
58. J.W. Brooks, M.H. Loretto, and R.E. Smallman: *Acta Metall.*, 1979, vol. 27, pp. 1839–47.
59. H. Idrissi, L. Ryelandt, M. Veron, D. Schryvers, and P.J. Jacques: *Scr. Mater.*, 2009, vol. 60, pp. 941–44.
60. D. Kuhlmann-Wilsdorf: *Mater. Sci. Eng. A.*, 1989, vol. 113, pp. 1–41.